Repository of the Max Delbrück Center for Molecular Medicine (MDC) in the Helmholtz Association

https://edoc.mdc-berlin.de/21121/

Diffusion-weighted magnetic resonance imaging in rat kidney using two-dimensional navigated, interleaved echo-planar imaging at 7.0 T

Liu Q., Xu Z., Zhao K., Hoge W.S., Zhang X., Mei Y., Lu Q., Niendorf T., Feng Y.

Diffusion-weighted MRI in rat kidney using 2D-navigated interleaved echo-planar imaging at 7.0 T

Qiang Liu[1,2,3], Zhongbiao Xu[4], Kaixuan Zhao[1,2,3], W. Scott Hoge[5], Xinyuan Zhang[1,2,3], Yingjie Mei[1,2,3], Qiqi Lu[1,2,3], Thoralf Niendorf[6], and Yanqiu Feng[1,2,3,*]

[1]School of Biomedical Engineering, Southern Medical University, Guangzhou, China

[2]Guangdong Provincial Key Laboratory of Medical Image Processing & Guangdong Province Engineering Laboratory for Medical Imaging and Diagnostic Technology, Southern Medical University, Guangzhou, China

[3]Guangdong-Hong Kong-Macao Greater Bay Area Center for Brain Science and Brain-Inspired Intelligence & Key Laboratory of Mental Health of the Ministry of Education, Southern Medical University, Guangzhou, China

[4]Department of Radiation Oncology, Guangdong Provincial People's Hospital, Guangdong Academy of Medical Sciences, Guangzhou, China

[5]Department of Radiology, Brigham and Women's Hospital, Harvard Medical School, Boston, MA, USA

[6]Berlin Ultrahigh Field Facility (B.U.F.F.), Max Delbrueck Center for Molecular Medicine in the Helmholtz Association, Berlin, Germany

Correspondence:

Yanqiu Feng, Ph.D., School of Biomedical Engineering, Southern Medical University, Guangzhou, China. Email: foree@163.com

Abbreviations：

2D, two-dimensional; ADC, apparent diffusion coefficient; CAT, combined acquisition techniques; CNR, contrast-to-noise ratio; DTI, diffusion-tensor imaging; DWI, diffusion-weighted imaging; EPI, echo-planar imaging; FA, fractional anisotropy; FOV, field of view; IRIS, image reconstruction using image-space sampling function; MD, mean diffusivity; ms-EPI, multi-shot EPI; PF, partial Fourier; PI, parallel imaging; RARE, rapid acquisition with relaxation enhancement; ROI, region of interest; SNR, signal-to-noise ratio; ss-EPI, single-shot EPI;

ABSTRACT

The purpose of this study was to investigate the feasibility of 2D-navigated interleaved multishot EPI to enhance kidney diffusion-weighted imaging (DWI) in rats at 7.0 T. Fully sampled interleaved 4-shot EPI with two-dimensional navigators was tailored for kidney DWI (Sprague-Dawley rats, n=7) on a 7T animal scanner. Image quality of 4-shot EPI was compared with T_2-weighted RARE (reference), single-shot EPI (ss-EPI) without and with parallel imaging (PI), contrast-to-noise ratio (CNR) was quantified on three EPI sequences. Dice similarity coefficient, and the Hausdorff distance were used for evaluation of image distortion. Mean diffusivity (MD) and fractional anisotropy (FA) were calculated for renal cortex and medulla for all DWI approaches. The corticomedullary difference of MD and FA were assessed (Wilcoxon signed-rank test). Four-shot EPI showed the highest CNR among three variants and the lowest geometric distortion versus T_2-weighted RARE (mean Dice: 0.77 for ss-EPI without PI, 0.88 for ss-EPI with twofold undersampling, and 0.92 for 4-shot EPI). The FA map derived from 4-shot EPI clearly identified a highly anisotropic region corresponding to the inner stripe of the outer medulla. Four-shot EPI successfully discerned differences in both MD and FA between renal cortex and medulla. In conclusion, 2D navigated, interleaved multi-shot EPI facilitates high-quality rat kidney DWI with clearly depicted intra- and inter layer structure and substantially reduced image distortion. This approach permits anatomic integrity of DWI and has the potential to benefit the characterization of renal microstructure in preclinical studies. (238)

INTRODUCTION

Diffusion-weighted imaging (DWI) is a non-invasive magnetic resonance imaging (MRI) technique sensitive to Brownian water motion in biological tissues. Kidney DWI provides information about the microstructural integrity and function of renal tissues.[1] Quantitative parameters derived from diffusion MRI, such as apparent diffusion coefficient (ADC) or mean diffusivity (MD) are instrumental for the assessment of diffuse renal pathologies, including renal fibrosis,[2,3] renal artery stenosis,[4] and renal transplant dysfunction.[5] By employing multiple diffusion encoding directions, diffusion-tensor imaging (DTI) is used to characterize the anisotropic diffusion nature in renal tissues.[6] The anisotropy pattern is explicit in the renal medulla which is mainly composed of radially distributed vessels, tubules, and collecting ducts. Previous studies showed that fractional anisotropy (FA) derived from DTI was higher in the healthy renal medulla than in the renal cortex.[7,8]

DWI is commonly acquired using single-shot echo-planar imaging (ss-EPI) because of its speed advantage and its motion insensitivity. In current practice, ss-EPI is the workhorse for kidney DWI.[9] Owing to the low bandwidth along the phase-encoding direction, renal DWI with ss-EPI is prone to distortion artifacts caused by susceptibility differences between the kidney and surrounding air or in kidney regions in close proximity to skin/fat/muscle boundaries.[10] The relatively long echo train duration used in ss-EPI usually results in blurring artifacts and thus limits spatial resolution, especially in the presence of a rapid T_2^* decay.[11] Geometric distortion and point spread function induced blurring in EPI can be reduced by incorporating parallel imaging (PI) techniques.[12-14]

Multi-shot EPI (ms-EPI) is an alternate approach to improve the geometric fidelity of DWI. This technique distributes the acquisition of the k-space data across multiple shots each covering a dedicated k-space segment along the frequency-encoding (readout-segmented ms-EPI)[15] or the phase-encoding (interleaved ms-EPI)[16,17] direction. The interleaved ms-EPI approach effectively increases the bandwidth along the phase-encoding direction and thus reduces geometric distortion. However, ms-EPI DWI may be contaminated with ghosting artifacts caused by inter-shot phase inconsistencies which result from motion-induced phase

accrual during the diffusion sensitizing or imaging gradients.[18] Adding a navigator echo after the image echo can be used to estimate and compensate for the inter-shot phase differences.[19,20] Previous studies demonstrated that readout-segmented ms-EPI in conjunction with two-dimensional (2D) navigator correction enhances the quality of renal DWI of human subjects and rodents on 3T clinical MR scanners.[21,22] Several studies have shown the capability of ms-EPI in obtaining high quality murine diffusion imaging, including placental perfusion,[23] mouse cervical spinal cord DWI,[24] mouse brain DTI.[25,26] So far, ms-EPI approaches have not been established for renal DWI at higher magnetic field strengths using preclinical small bore MR instruments, where susceptibility gradients might be pronounced and where the enhanced gradient coil performance reduces the duration of the diffusion sensitizing gradient pulses and affords shorter echo times.

Recognizing the challenge and opportunity this work examines the feasibility of multi-shot EPI interleaved along the phase-encoding direction to enhance renal DWI in rats using a 7.0 T preclinical animal scanner. For this purpose, extra navigator echoes were implemented to correct inter-shot phase variations in interleaved ms-EPI. Image quality of diffusion sensitized ms-EPI of the rat kidney was systematically evaluated by contrast-to-noise ratio (CNR) and distortion level[27] for benchmarking against single-shot DWI-EPI. Differences in mean diffusivity and fractional anisotropy between renal cortex and medulla were compared for the employed DWI-EPI variants.

METHODS

Animals

This study was approved by the local Institutional Animal Care and Use Committee. Seven male Sprague-Dawley rats (aged 7-8 weeks, bodyweight 150-180 g) were involved. The animals had ad libitum access to standard diet food and water while housed under standard conditions with environmental enrichment. During MRI scanning, 1.5% isoflurane was employed for animal anesthesia. Body temperature was maintained at 38°C with a circulating water blanket (Thermo Haake, Karlsruhe, Germany) placed on the rat's abdomen. Respiration rate was monitored throughout the experiment (SA Instruments, New York, NY, USA).

Imaging acquisition

All MRI experiments were carried out on a 7.0 T, 16 cm bore animal MR scanner equipped with a 90 mm gradient and shim coil set (B-GA9S HP), capable of generating maximum gradient amplitude of 760 mT/m each axis and slew rate of 6840 T/m/s (PharmaScan; Bruker BioSpin, Ettlingen, Germany). A 72 mm diameter volume RF coil was used for spin excitation in conjunction with a four-channel surface RF coil array (outer diameter: 68 mm, length: 590 mm) used for signal reception (Bruker BioSpin, Ettlingen, Germany). Respiratory triggering was used to minimize the effect of respiratory motion.

T_2-weighted (T2W) 2D RARE (TR=3000 ms, TE=20 ms, RARE factor=8, number of slices=1, slice thickness=2 mm, field of view (FOV)=40×55 mm^2, matrix size=150×150, in-plane spatial resolution=0.27×0.37 mm^2, receiver bandwidth=78,125 Hz, number of averages=2, and total scan time=1 min 48 s) was first performed for localization and for obtaining the anatomical reference used for the assessment of geometric distortions. B_0 field map-based shimming was performed to minimize B_0 field inhomogeneity.

The scanning parameters used for all three DWI-EPI variants were: TR=3000 ms, receiver bandwidth=200,000 Hz, FOV=40×55 mm^2, matrix size=128×96, in-plane spatial resolution=0.31×0.57 mm^2, slice thickness=2 mm, number of averages=4, eight diffusion-directions at b=500 s/mm^2 (the maximum gradient strength and gradient scaling

were 200.3 mT/m and 51.6% per channel, diffusion gradient duration (δ) was 4.5 ms, and diffusion gradient separation (Δ) was 10.6 ms) and at b=0 s/mm^2 image. SS-EPI sequences (partial Fourier (PF) factor=5/8, total scan time=1 min 48 s) were performed without (R=1, TE=32.01 ms) and with PI (R=2, TE=24.49 ms). Supplementary Material Figure 1 presents the sequence diagram and the corresponding k-space trajectory of the implemented 2D navigated ms-EPI sequence (number of shots=4, TE=32.66 ms, TE of the navigator=58.08 ms, matrix size of the navigator=32×24, spatial resolution of the navigator=1.25×2.29 mm^2, PF-factor=1, total scan time=7 min 12 s, protocol name: 4-shot EPI), the echo spacing of the navigator-echo was reduced by 4 times to ensure consistent acquisition bandwidths (6250 Hz along PE direction) between the image and the navigator echoes, to make sure that the distortion level of navigator echo matches that of the image echo.[28] To mitigate the chemical-shift artifact, fat suppression was conducted for all the three EPI variants.

Image reconstruction

Image reconstruction and calculation of the evaluation metrics were performed in Matlab 2016b (MathWorks, Natick, MA, USA). GRAPPA was used for the reconstruction of the undersampled data.[14] For ss-EPI variants, data from PF acquisition were reconstructed using homodyne reconstruction.[29] Image Reconstruction using Image-space Sampling function (IRIS) was used for the reconstruction of the ms-EPI data.[16] First, the navigator-echo k-space data were interpolated by cubic spline interpolation to the size of the image-echo and then inverse Fourier transformed to obtain a complex navigator-echo image. The phase of the complex image was served as the extra phase Φ_m induced by subject motion during the diffusion sensitization period, separately from each shot. The extra-phase information Φ_m was then incorporated into the encoding matrix E, which combines the encoding matrix containing motion-induced phase ($P_{j,s}$, a diagonal matrix whose principal diagonal elements equals to $\exp(i\Phi_m)$), coil sensitivity ($S_{j,c}$), and the shifting of k-space sampling (A_s):

$$E_{j,c,s} = A_s S_{j,c} P_{j,s} \tag{1}$$

where j represents each phase-encoding step, c the number of coil channels, and s the number of shots. Then the reconstruction of the image-echo image $\hat{f}$ follows:[16]

$$\hat{f} = \left(E^H \psi^{-1} E \right)^{-1} E^H \psi^{-1} g, \qquad (2)$$

where ψ represents the noise correlation matrix, g the aliased image which is generated from the inverse Fourier transform of the undersampled k-space data, and H the Hermitian transposed complex conjugate operator.

Evaluation metrics

Contrast-to-noise ratio

The contrast-to-noise ratio (CNR) was analyzed for ss-EPI and ms-EPI images at b=0 s/mm^2. One 25-pixel circular ROI was placed in the inner medulla (IM) of the kidney and the other is manually drawn as large as possible within the inner stripe of the outer medulla (ISOM), CNR was defined as the absolute signal difference of ISOM and IM divided by the standard deviation of IM (Ref. 30):

$$CNR = \frac{|S_{ISOM} - S_{IM}|}{SD_{IM}}. \qquad (3)$$

Geometric distortion

The evaluation of geometric distortion was performed following the approach reported by Periquito, et al.[27] First, the kidney outlines were manually segmented in T2W RARE images to define the distortion-free reference. Subsequently, the reference contours were superimposed to non-diffusion sensitized images of ss-EPI and 4-shot EPI acquisitions. The explicit illustration of the distortion levels was presented in color-coded difference-maps between the kidney outlines derived from ss-EPI and 4-shot EPI acquisitions and the T2W RARE reference. The Dice similarity coefficient and the Hausdorff distance were computed for quantitative evaluation of image distortion.

Mean diffusivity and fractional anisotropy

Using a monoexponential signal decay model, the diffusion tensor was first calculated for each pixel. MD and FA were calculated based on the eigenvalues (λ_1, λ_2, λ_3) of the tensor according to Refs. 31 and 32.

Statistical analysis

All animals scanned were included in the data analysis. MD and FA were compared between renal cortex and renal medulla using Wilcoxon signed-rank test. All statistical analyses were performed in SPSS (v.19.0, SPSS Inc, Chicago, IL). $P<0.05$ was considered as statistically significant.

RESULTS

Figure 1 presents representative images derived from 4-shot EPI, ss-EPI without (R=1) and with parallel imaging (R=2), and T2W RARE. The anatomic fidelity of the images obtained with fully sampled ss-EPI was compromised by severe geometric distortion and susceptibility artifacts. Image quality was improved by introducing PI undersampling (R=2), whereas the susceptibility artifact was still pronounced near the air cavity as pointed by the red arrows. Unlike the ss-EPI variants, 2D navigated 4-shot EPI yielded significantly reduced geometric distortion, clearly defined renal outline and anatomic representation of the renal layers and intrarenal structures.

The quantitative results of the evaluation metrics including CNR, the Dice similarity coefficient, and the Hausdorff distance are summarized in Table 1. The 4-shot EPI achieved the highest CNR value among three variants. The corresponding Dice similarity coefficients were 0.77±0.07, 0.87±0.04, and 0.92±0.03 for conventional ss-EPI, two-fold undersampled ss-EPI, and navigated 4-shot EPI. The 4-shot EPI variant obtained the lowest Hausdorff distance.

An illustrative assessment of geometric distortion is provided in Figure 2. Figure 2A shows the kidney contours manually segmented for T2W RARE images. These reference contours are superimposed to the images derived from ss-EPI and navigated 4-shot EPI. The reference contours match the kidneys in the 4-shot EPI image better than those in the ss-EPI images. The difference map provided in Figure 2B demonstrates less geometric distortion for 4-shot EPI versus ss-EPI.

Figure 3 displays the quantitative MD and FA maps obtained for the three EPI variants. The MD maps derived from 4-shot EPI reveal heterogenous interlayer and uniform intralayer patterns that are consistent with renal anatomy. The FA maps obtained for 4-shot EPI data demonstrate a higher degree of diffusion anisotropy in the inner stripe of the outer medulla

than in the outer stripe of the outer medulla, the inner medulla, and the renal cortex. This anisotropy pattern was not observed in the FA map derived from ss-EPI images. Besides, we observed abnormally high values at the boundary of the kidney in the FA map derived from ss-EPI images.

Figure 4 shows representative regions of interest (ROIs) covering the renal cortex and medulla. The ROIs were obtained from ms-EPI (b=0 s/mm^2) and superimposed to the corresponding MD map. A comparison of the MD and FA values obtained for the renal cortex and medulla for all animals is shown in Figure 5 for the three DWI-EPI approaches. For 4-shot EPI, MD was significantly higher in the cortex than in the medulla (1.44×10^{-3} mm^2/s vs 1.39×10^{-3} mm^2/s, P=0.008), while FA was significantly lower in the cortex than in the medulla (0.20 vs 0.27, P<0.001). These significant differences were not consistently observed for the ss-EPI variants. The application of ss-EPI (R=1) only revealed the corticomedullary difference in MD (1.36×10^{-3} mm^2/s vs 1.23×10^{-3} mm^2/s, P=0.008). For two-fold undersampled ss-EPI, no corticomedullary difference was detected in either MD or FA maps.

DISCUSSION

This study demonstrates the applicability of navigated ms-EPI to enhance rat kidney DWI on a 7.0 T animal scanner. Compared with conventional ss-EPI variants, 2D navigated interleaved ms-EPI achieved renal DWI with clearly depicted intra- and inter layer structure and significantly reduced geometric distortion. The renal FA map derived from ms-EPI showed a well-defined region with highly anisotropic diffusion properties in the inner stripe of the outer medulla. Our results also demonstrate that ms-EPI outperforms ss-EPI in the ability to detect the corticomedullary differentiation in diffusion parameters such as MD and FA.

A significant improvement of ms-EPI over ss-EPI is the reduction of geometric distortion and enhancement in anatomic fidelity. The amount of local distortion in EPI is proportional to the B_0 field inhomogeneity and inversely proportional to the bandwidth in the phase-encoding direction. The severe distortion observed in fully sampled ss-EPI based renal imaging was caused by the inhomogeneous B_0 field at the interface of the kidney margin. Consistent with previous reports,[9,12] our results show that distortion in EPI can be reduced by using parallel imaging, which increases the bandwidth along the phase-encoding direction by increasing the k-space distance between neighboring phase-encoding lines. A two-fold undersampling corresponds to two times of the bandwidth in the phase-encoding direction. Further increase of undersampling would benefit the reduction of geometric distortion at the cost of noise amplification and residual aliasing artifacts. The interleaved 4-shot EPI acquisition adopted in this study increases the bandwidth in the phase-encoding direction by a factor of four versus fully sampled ss-EPI. Consequently, the spatial displacement caused by B_0 inhomogeneities in 4-shot EPI is only half of that induced in two-fold accelerated ss-EPI. This gain in anatomic fidelity is reflected by the renal difference maps, the Dice coefficients and the Hausdorff distance obtained for the three EPI variants.

The evaluated CNR and geometric integrity of ms-EPI images facilitate a clear depiction of the renal outline and the intrarenal anatomic structure, which benefit the accurate definition of the main renal layers and the assignment of anatomic ROIs. The improved image quality

obtained for ms-EPI benefits the calculation of quantitative diffusion-related parameters. Our results demonstrated that ms-EPI outperformed ss-EPI in detecting the inter-layer differences in mean diffusivity and fractional anisotropy. Interestingly, a region with high FA values was identified in the inner stripe of the outer medulla in the FA map derived 4-shot EPI, while this observation was not made for the ss-EPI based FA maps. The radially-orientated tubular structures in the medulla probably contribute to the preferred diffusion direction and high FA values.[6,33,34] Previous studies showed that FA decreases in regions where renal impairment occurs.[35-38] Note that FA values near the kidney boundaries were abnormally high in the ss-EPI variants. This can be explained by the fact that eddy-current induced distortions are diffusion direction-dependent,[39] as shown in Supplementary Material Figure 2. The reduced distortion of interleaved 4-shot EPI sequence over ss-EPI variants contributes to improve the accuracy and robustness in FA quantification. These findings suggest that ms-EPI might play an important role in the preclinical research of renal diseases associated with changes in micromorphology and water diffusion.

Alternative methods to improve DWI of the kidney include RARE and readout-segmented ms-EPI. RARE includes a series of refocusing pulses which making it insensitive to B0-inhomogeneities, and thus provides high anatomic accuracy. Directly applying diffusion-sensitizing gradients to RARE sequence may face the issue that motion during the diffusion-sensitizing gradients would make the sequence violate the Carr-Purcell-Meiboom-Gill (CPMG) condition,[40] which leads to signal loss and error in diffusion measurement. Split-echo RARE[27] method successfully addresses this problem and improves the anatomic integrity of renal DWI. The train of refocusing pulses results in an imaging speed and RF power deposition handicap over EPI.[41] To address these constraints, Combined Acquisition Techniques (CAT)[42] have been applied to boost imaging speed and to reduce RF power deposition by using a modular hybrid approach that integrates RARE and EPI.[43-45] A RARE-EPI hybrid is conceptually appealing for the pursuit of renal DWI at (ultra)high fields due to the anatomic integrity of RARE in conjunction with the imaging speed and RF power deposition advantage of EPI.[46]

Another approach of multi-shot DWI is readout-segmented ms-EPI where k-space segmentation occurs along the frequency-encoding direction. Given the same k-space coverage, readout-segmentation improves the phase-encoding sampling bandwidth. However, more data acquisition occurs during gradient ramping, compared with interleaved ms-EPI employed in this work. As a result, the actual distortion reduction in readout-segmented EPI deviates negatively from the ideal reduction. This deviation increases with the number of segments.[47,48] Thus, the readout-segmented approach is less effective in distortion reduction than the interleaved ms-EPI approach, especially as the number of segments increases.

Phase inconsistencies in multi-shot acquisitions can also be addressed by self-navigated approaches such as multiplexed sensitivity-encoding (MUSE)[49] and self-navigated interleaved spiral (SNAILS)[50]. SNAILS is based on multishot variable-density spiral readout trajectory and employs data in the oversampled k-space center as navigator for inter-shot motion correction. The reconstruction of non-Cartesian data in SNAILS usually requires sophisticated and time-consuming algorithms. In addition, the actual k-space sampling trajectory may deviate from the prescribed one because of gradient imperfections.[51] MUSE is based on an interleaved-multishot EPI sequence, and it adopts a two-step SENSE reconstruction procedure to correct the motion-induced phase errors between interleaves. Each interleave is first reconstructed using SENSE. The phase of individual interleaves was used to modulate coil sensitivities and incorporated into the final SENSE reconstruction of all interleaves. Recently developed autocalibrating segmented diffusion-weighted acquisitions (ASeDiWA)[52] can be seen as a GRAPPA variant of the MUSE algorithm, which enables an iteration of the reconstruction procedure, this variant has been initially investigated for its improvement of phase estimation in preclinical settings. The number of shots in MUSE related approaches is limited by the number of array coils and the performance of parallel reconstruction. In preclinical context where only few receiver coils are available, the utility of this approach is limited.[53] In contrast, there is no limitation on the number of interleaves in the navigator-based approach adopted in our work.

A limitation of the present work is the scan time prolongation of 2D navigated ms-EPI versus

ss-EPI. The ms-EPI approach was implemented with a fully sampled acquisition in our experiments. To compensate for the scan time prolongation parallel imaging techniques can be integrated in ms-EPI. Furthermore, combining blip-up/down acquisition (BUDA) strategy with ms-EPI has the potential to achieve distortion-free renal DWI with high-resolution.[54,55] Only a half of 4 shots will be used in BUDA, compared to our 4-shot EPI settings, and thus reduces the scan time to half. Another drawback is the restricted spatial resolution along the slice direction. DTI is well established in the literature for renal DWI. The enhanced resolution of DWI reported here benefits the quantification of diffusion-related metrics and renal fiber tractography. Yet, the spatial resolution of 2D acquisitions is still limited in the slice direction due to SNR limitations. Combining ms-EPI with simultaneous multiple slab excitation, parallel imaging, and slice super-resolution techniques provides potential for improving the resolution of renal DWI in the slice direction.[37,56,57]

CONCLUSIONS

This study demonstrates the value of 2D navigated interleaved multishot EPI to enhance rat kidney DWI at high magnetic fields. The elevated CNR and improvement of geometric integrity facilitated by multishot EPI contributes to a clear depiction and delineation of intra-renal structures and benefits quantification of renal water diffusion-related metrics. The present study relies on normal rats as a prelude to studies in small rodent models. Renal DWI with 2D navigated interleaved ms-EPI will support preclinical studies and translational research aimed at further elucidating changes in water diffusion and micromorphology associated with renal pathology. It will also enable new insights into mechanisms of renal pathophysiology by means of systematic analysis of the relationship between fractional anisotropy and mean diffusivity probed with DWI and physiological measurements.

FIGURE LEGENDS

Figure 1. Comparison of in vivo images obtained with ss-EPI (wo/w parallel imaging) and with 4-shot EPI. T2W-RARE shown in the left column represents the anatomic reference. The medium column presents non-diffusion weighted images ($b = 0$ s/mm^2). The right column illustrates diffusion weighted (DW) images ($b = 500$ s/mm^2). The renal outline and intra-renal structure were more clearly depicted for 4-shot EPI versus ss-EPI. The red arrows indicate susceptibility artifacts in ss-EPI variants.

Table 1. Evaluation metrics of the image quality obtained by ss-EPI variants and the 4-shot EPI sequence, including Contrast-to-noise Ratio (CNR), the Dice similarity coefficient, and the Hausdorff distance.

Figure 2. Assessment of geometric distortion for the ss-EPI and 4-shot EPI variants. Reference outlines of the rat kidney were manually obtained from the T2W-RARE image (A). The red contours were then overlaid on the EPI images. The color-coded difference maps (B) with respect to the T2W-RARE reference demonstrate the amount of distortion. Blue represents false negative (-1), red indicates false positive (+1) against the reference. The Dice factors provide a quantitative metric for EPI image distortion versus the T2W-RARE reference.

Figure 3. Representative quantitative parameter maps including MD and FA derived from in vivo DWI of the rat kidney using ss-EPI (R = 1, left column), ss-EPI (R = 2, center column), and 4-shot EPI (right column).

Figure 4. Representative definition of regions of interest (ROI) for in vivo rat kidney. The blue and orange shadings indicate the ROIs of the renal cortex and the renal medulla in the right kidney. ROIs were manually drawn on the $b = 0$ s/mm^2 image and overlaid on the corresponding MD map.

Figure 5. Comparison of MD and FA parameters between renal cortex and renal medulla (N = 7). *, **, and *** denote that a Wilcoxon signed-rank test produced a *P*-value less than 0.05, 0.01, and 0.001, respectively.

Supplementary Material Figure 1. The sequence diagram (a) and the corresponding k-space trajectory (b) of the implemented 2D navigated ms-EPI sequence.

Supplementary Material Figure 2. All the diffusion-weighted images (8 in total) with the contours from *b*-value = 0 overlapped on them, for R = 1 ss-EPI (2A), R = 2 ss-EPI (2B), and 4-shot EPI (2C), respectively. The eddy-current induced distortions are pointed by the yellow arrows and the susceptibility artifacts are pointed by the green arrows. The mean diffusivity (MD) map and the fractional anisotropy (FA) map are presented in the first column.

References:

1. Thoeny HC, Zumstein D, Simon-Zoula S, et al. Functional Evaluation of Transplanted Kidneys with Diffusion-weighted and BOLD MR Imaging: Initial Experience. *Radiology*. 2006;241(3):812-821.

2. Togao O, Doi S, Kuro-o M, et al. Assessment of Renal Fibrosis with Diffusion-weighted MR Imaging: Study with Murine Model of Unilateral Ureteral Obstruction. *Radiology*. 2010;255(3):772-780.

3. Cai XR, Yu J, Zhou QC, et al. Use of intravoxel incoherent motion MRI to assess renal fibrosis in a rat model of unilateral ureteral obstruction. *J Magn Reson Imaging*. 2016;44(3):698-706.

4. Yildirim E, Kirbas I, Teksam M, et al. Diffusion-weighted MR imaging of kidneys in renal artery stenosis. *Eur J Radiol*. 2008;65(1):148-153.

5. Hueper K, Khalifa AA, Bräsen JH, et al. Diffusion-Weighted imaging and diffusion tensor imaging detect delayed graft function and correlate with allograft fibrosis in patients early after kidney transplantation. *J Magn Reson Imaging*. 2016;44(1):112-121.

6. Ries M, Jones RA, Basseau F, et al. Diffusion tensor MRI of the human kidney. *J Magn Reson Imaging*. 2001;14(1):42-49.

7. Fukuda Y, Ohashi I, Hanafusa K, et al. Anisotropic diffusion in kidney: apparent diffusion coefficient measurements for clinical use. *J Magn Reson Imaging*. 2000;11(2):156-160.

8. Wang W, Pui MH, Guo Y, et al. MR diffusion tensor imaging of normal kidneys. *J Magn Reson Imaging*. 2014;40(5):1099-1102.

9. Wang H, Cheng L, Zhang X, et al. Renal Cell Carcinoma: Diffusion-weighted MR Imaging for Subtype Differentiation at 3.0 T. *Radiology*. 2010;257(1):135-143.

10. Borrelli P, Cavaliere C, Basso L, et al. Diffusion Tensor Imaging of the Kidney: Design and Evaluation of a Reliable Processing Pipeline. *Sci Rep*. 2019;9(1):12789.

11. Qin Q. Point spread functions of the T2 decay in k-space trajectories with long echo train. *Magn Reson Imaging*. 2012;30(8):1134-1142.

12. Notohamiprodjo M, Glaser C, Herrmann KA, et al. Diffusion tensor imaging of the kidney with parallel imaging: initial clinical experience. *Invest Radiol*. 2008;43(10):677-685.

13. Pruessmann KP, Weiger M, Scheidegger MB, et al. SENSE: sensitivity encoding for fast MRI. *Magn Reson Med*. 1999;42(5):952-962.

14. Griswold MA, Jakob PM, Heidemann RM, et al. Generalized autocalibrating partially parallel acquisitions (GRAPPA). *Magn Reson Med*. 2002;47(6):1202-1210.

15. Porter DA, Heidemann RM. High resolution diffusion-weighted imaging using readout-segmented echo-planar imaging, parallel imaging and a two-dimensional navigator-based reacquisition. *Magn Reson Med*. 2009;62(2):468-475.

16. Jeong H, Gore JC, Anderson AW. High-resolution human diffusion tensor imaging using 2-D navigated multishot SENSE EPI at 7 T. *Magn Reson Med*. 2013;69(3):793-802.

17. Xu Z, Huang F, Wu Z, et al. Technical Note: Clustering-based motion compensation scheme for multishot diffusion tensor imaging. *Med Phys*. 2018;45(12):5515-5524.

18. Butts K, de Crespigny A, Pauly JM, et al. Diffusion-weighted interleaved echo-planar imaging with a pair of orthogonal navigator echoes. *Magn Reson Med*. 1996;35(5):763-770.

19. Wu D, Lei J, Rosenzweig JM, et al. In utero localized diffusion MRI of the embryonic mouse brain microstructure and injury. *J Magn Reson Imaging*. 2015;42(3):717-728.

20. Cai Y, McMurray MS, Oguz I, et al. Use of High Resolution 3D Diffusion Tensor Imaging to Study

Brain White Matter Development in Live Neonatal Rats. *Front Psychiatry*. 2011;2:54.

21. Friedli I, Crowe LA, Viallon M, et al. Improvement of renal diffusion-weighted magnetic resonance imaging with readout-segmented echo-planar imaging at 3T. *Magn Reson Imaging*. 2015;33(6):701-708.

22. Wu C, Wang Q, Zhang J, et al. Readout-segmented echo-planar imaging in diffusion-weighted imaging of the kidney: comparison with single-shot echo-planar imaging in image quality. *Abdom Radiol*. 2016;41(1):100-108.

23. Alison M, Chalouhi GE, Autret G, et al. Use of Intravoxel Incoherent Motion MR Imaging to Assess Placental Perfusion in a Murine Model of Placental Insufficiency. *Invest Radiol*. 2013;48(1):17-23.

24. Callot V, Duhamel G, Cozzone PJ, et al. Short-scan-time multi-slice diffusion MRI of the mouse cervical spinal cord using echo planar imaging. *NMR Biomed*. 2008;21(8):868-877.

25. Guilfoyle DN, Gerum S, Hrabe J. Murine diffusion imaging using snapshot interleaved EPI acquisition at 7T. *J Neurosci Meth*. 2011;199(1):10-14.

26. Langhauser FL, Heiler PM, Grudzenski S, et al. Thromboembolic stroke in C57BL/6 mice monitored by 9.4 T MRI using a 1H cryo probe. *Exp Transl Stroke Med*. 2012;4(1):18.

27. Periquito J, Paul K, Huelnhagen T, et al. Diffusion-weighted Renal MRI at 9.4 Tesla Using RARE to Improve Anatomical Integrity. *Sci Rep*. 2019;9(1):19723.

28. Liu W, Zhao X, Ma Y, et al. DWI using navigated interleaved multishot EPI with realigned GRAPPA reconstruction. *Magn Reson Med*. 2016;75(1):280-286.

29. Noll DC, Nishimura DG, Macovski A. Homodyne detection in magnetic resonance imaging. *IEEE Trans Med Imaging*. 1991;10(2):154-163.

30. An H, Ma X, Pan Z, et al. Qualitative and quantitative comparison of image quality between single-shot echo-planar and interleaved multi-shot echo-planar diffusion-weighted imaging in female pelvis. *Eur Radiol*. 2020;30(4):1876-1884.

31. Kingsley PB. Introduction to diffusion tensor imaging mathematics: Part II. Anisotropy, diffusion-weighting factors, and gradient encoding schemes. *Concepts in Magnetic Resonance Part A*. 2006;28A(2):123-154.

32. Kingsley PB. Introduction to diffusion tensor imaging mathematics: Part III. Tensor calculation, noise, simulations, and optimization. *Concepts in Magnetic Resonance Part A*. 2006;28A(2):155-179.

33. Kataoka M, Kido A, Yamamoto A, et al. Diffusion tensor imaging of kidneys with respiratory triggering: Optimization of parameters to demonstrate anisotropic structures on fraction anisotropy maps. *J Magn Reson Imaging*. 2009;29(3):736-744.

34. Özkan MB, Marterer R, Tscheuner S, et al. The role of kidney diffusion tensor magnetic resonance imaging in children. *Egypt J Radiol Nucl Med*. 2016;47(4):1599-1611.

35. Donnola SB, Piccone CM, Lu L, et al. Diffusion tensor imaging MRI of sickle cell kidney disease: initial results and comparison with iron deposition. *NMR Biomed*. 2018;31(3):e3883. https://doi.org/10.1002/nbm.3883

36. Gaudiano C, Clementi V, Busato F, et al. Diffusion tensor imaging and tractography of the kidneys: assessment of chronic parenchymal diseases. *Eur Radiol*. 2013;23(6):1678-1685.

37. Feng Q, Ma Z, Wu J, et al. DTI for the assessment of disease stage in patients with glomerulonephritis - correlation with renal histology. *Eur Radiol*. 2015;25(1):92-98.

38. Cheung JS, Fan SJ, Chow AM, et al. Diffusion tensor imaging of renal ischemia reperfusion injury in an experimental model. *NMR Biomed*. 2010;23(5):496-502.

39. Irfanoglu MO, Sarlls J, Nayak A, et al. Evaluating corrections for Eddy-currents and other EPI distortions in diffusion MRI: methodology and a dataset for benchmarking. *Magn Reson Med*. 2018;81(4):2774-2787.

40. Norris DG, Börnert P, Reese T, et al. On the application of ultra-fast RARE experiments. *Magn Reson Med*. 1992;27(1):142-164.

41. Schick F. SPLICE: sub-second diffusion-sensitive MR imaging using a modified fast spin-echo acquisition mode. *Magn Reson Med*. 1997;38(4):638-644.

42. Hillenbrand C, Hahn D, Haase A, et al. MR CAT scan: a modular approach for hybrid imaging. *Magn Reson Mater Phys Biol Med*. 2000;10(3):183-199.

43. Hillenbrand C, Sandstede J, Pabst T, et al. Hybrid cardiac imaging with MR-CAT scan: a feasibility study. *J Magn Reson Imaging*. 2000;11(6):711-716.

44. Jakob PM, Hillenbrand CM, Kenn W, et al. Abdominal imaging with a modular combination of spin and gradient echoes. *Magn Reson Med*. 2002;47(3):425-432.

45. Choli M, Blaimer M, Breuer FA, et al. Combined acquisition technique (CAT) for high-field neuroimaging with reduced RF power. *Magn Reson Mater Phys Biol Med*. 2013;26(4):411-418.

46. Paul K, Huelnhagen T, Oberacker E, et al. Multiband diffusion-weighted MRI of the eye and orbit free of geometric distortions using a RARE-EPI hybrid. *NMR Biomed*. 2018;31(3).

47. Wang Y, Ma X, Zhang Z, et al. A comparison of readout segmented EPI and interleaved EPI in high-resolution diffusion weighted imaging. *Magn Reson Imaging*. 2018;47:39-47.

48. Holdsworth SJ, Skare S, Newbould RD, et al. Readout-segmented EPI for rapid high resolution diffusion imaging at 3 T. *Eur J Radiol*. 2008;65(1):36-46.

49. Chen N, Guidon A, Chang H, et al. A robust multi-shot scan strategy for high-resolution diffusion weighted MRI enabled by multiplexed sensitivity-encoding (MUSE). *NeuroImage*. 2013;72:41-47.

50. Liu C, Bammer R, Kim D, et al. Self-navigated interleaved spiral (SNAILS): Application to high-resolution diffusion tensor imaging. *Magn Reson Med*. 2004;52(6):1388-1396.

51. Wilm BJ, Barmet C, Gross S, et al. Single-shot spiral imaging enabled by an expanded encoding model: Demonstration in diffusion MRI. *Magn Reson Med*. 2017;77(1):83-91.

52. Herbst M. Autocalibrating segmented diffusion-weighted acquisitions. *Magn Reson Med*. 2021;86(4):1997-2010.

53. Hu Y, Ikeda DM, Pittman SM, et al. Multishot Diffusion-Weighted MRI of the Breast With Multiplexed Sensitivity Encoding (MUSE) and Shot Locally Low-Rank (Shot-LLR) Reconstructions. *J Magn Reson Imaging*. 2021;53(3):807-817.

54. Liao C, Bilgic B, Tian Q, et al. Distortion-free, high-isotropic-resolution diffusion MRI with gSlider BUDA-EPI and multicoil dynamic B0 shimming. *Magn Reson Med*. 2021;86(2):791-803.

55. Afacan O, Hoge WS, Wallace TE, et al. Simultaneous Motion and Distortion Correction Using Dual-Echo Diffusion-Weighted MRI. *J Neuroimaging*. 2020;30(3):276-285.

56. Chang H, Sundman M, Petit L, et al. Human brain diffusion tensor imaging at submillimeter isotropic resolution on a 3 Tesla clinical MRI scanner. *NeuroImage*. 2015;118:667-675.

57. Wu W, Poser BA, Douaud G, et al. High-resolution diffusion MRI at 7T using a three-dimensional multi-slab acquisition. *NeuroImage.* 2016;143:1-14.

Table 1 Evaluation metrics of the image quality obtained by ss-EPI variants and the 4-shot EPI sequence, including Contrast-to-noise Ratio (CNR), the Dice similarity coefficient, and the Hausdorff distance.

	CNR	Dice	Hausdorff distance
ss-EPI R=1	4.31±1.37	0.77±0.07	4.26±0.60
ss-EPI R=2	4.00±1.94	0.87±0.04	3.46±0.44
4-shot EPI	**7.66±1.91**	**0.92±0.03**	**2.81±0.35**

New figure 1

New figure 2

(A)

| T2W-RARE | ss-EPI R = 1 | ss-EPI R = 2 | 4-shot EPI |

(B)

+1 False Positive
0 Same
-1 False Negative

Dice = 0.70   Dice = 0.84   Dice = 0.87
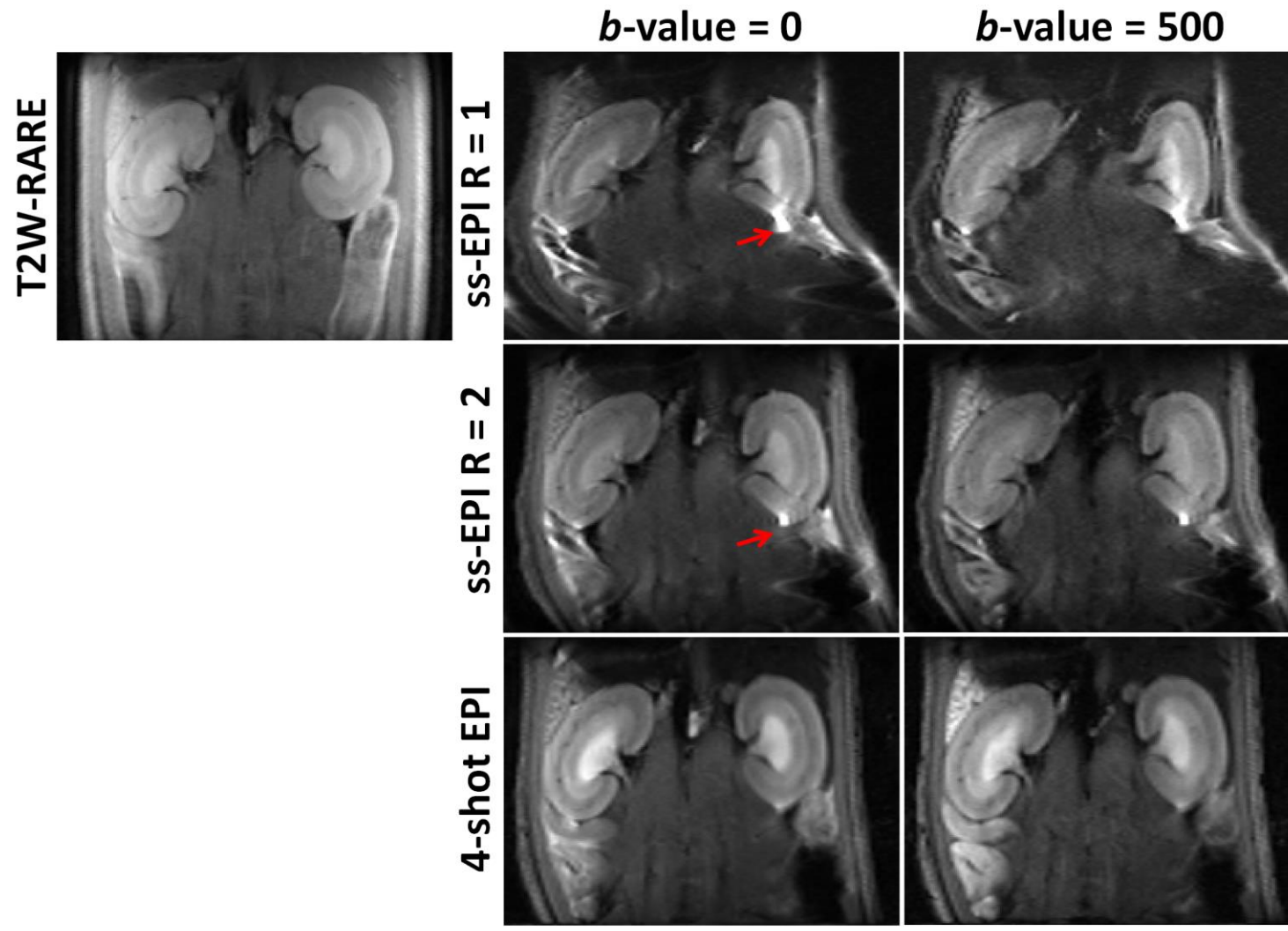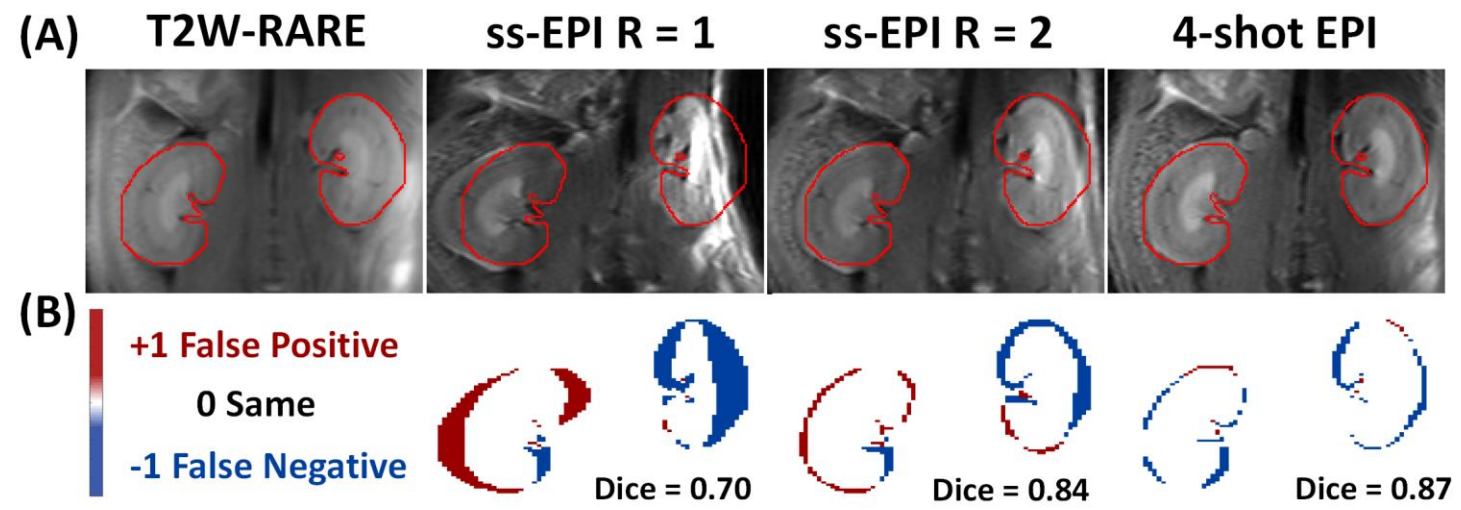
New figure 3

figure 4

New figure 5

Mean Diffusivity

10^{-3} mm²/s

** (ss-EPI R = 1)
** (4-shot EPI)

Fractional Anisotropy

*** (4-shot EPI)

Cortex
Medulla

(A)

(B)
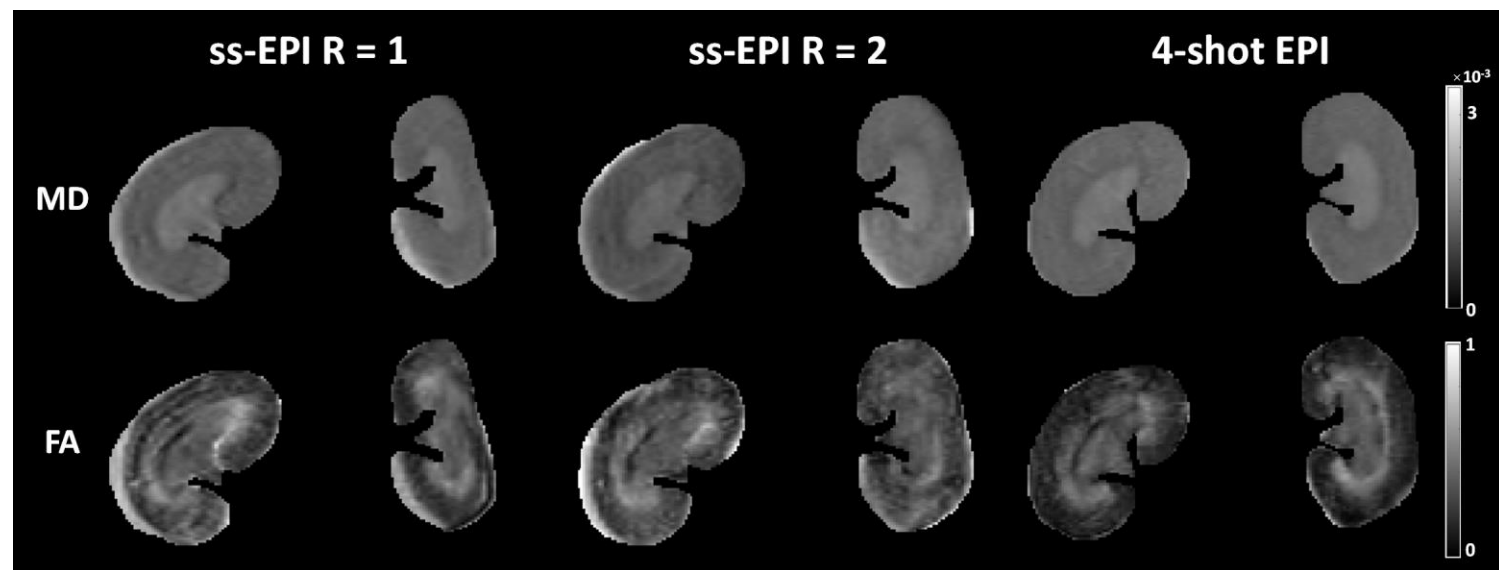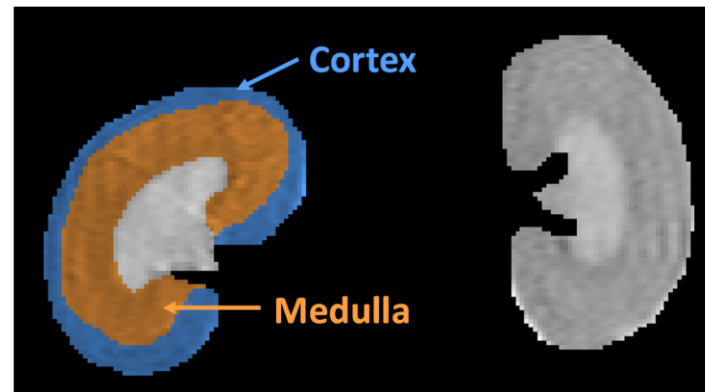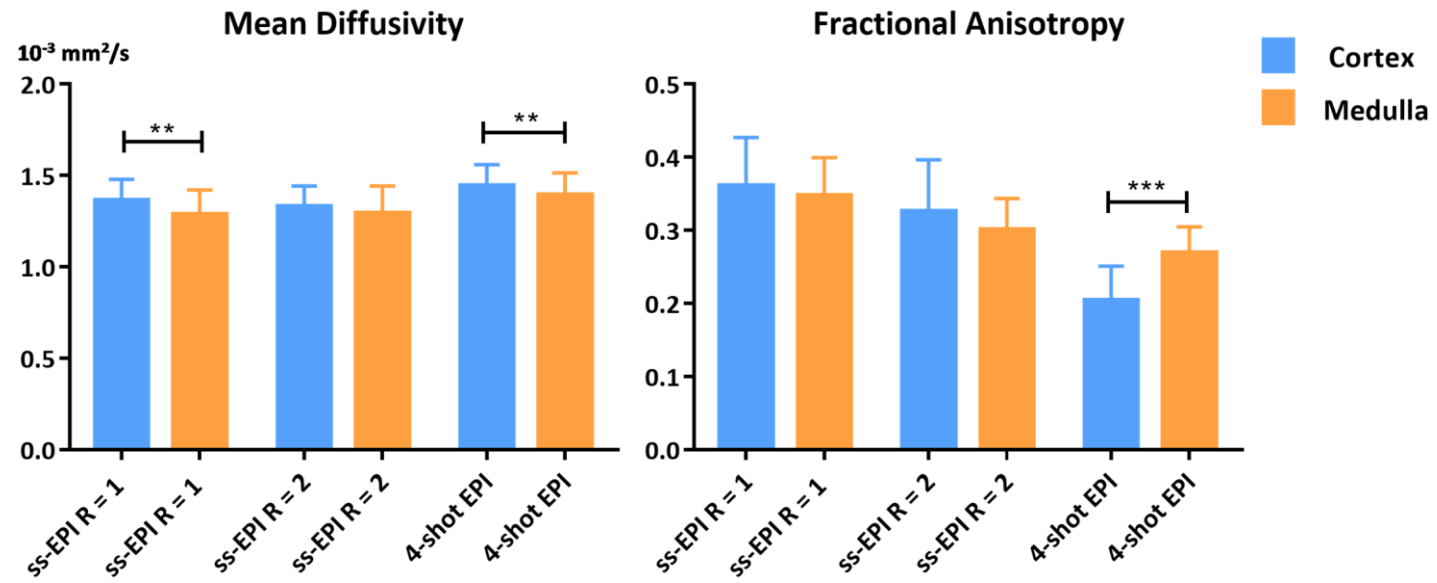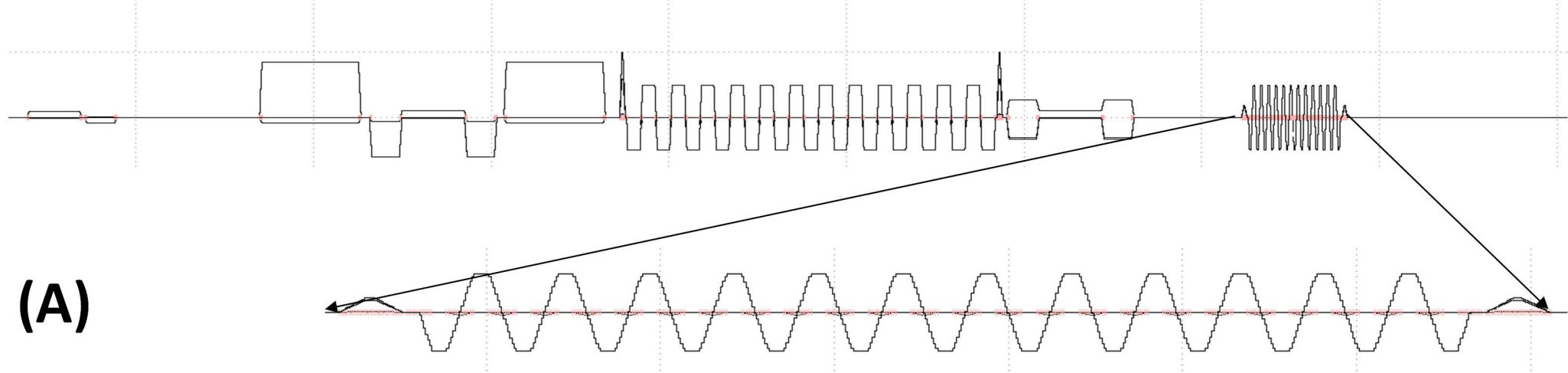
	1st shot	2nd shot	3rd shot	4th shot
image-echo				
navigator-echo				
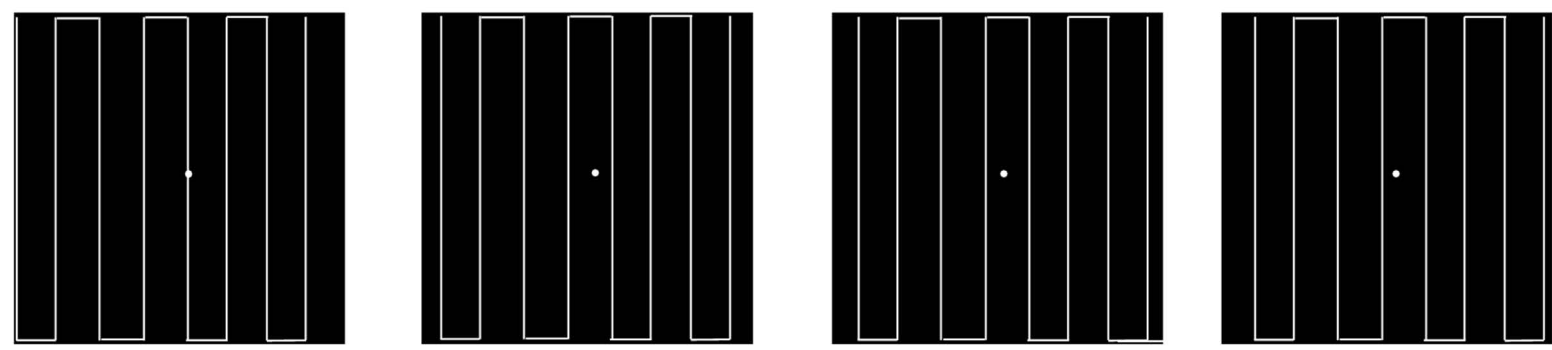
(A) **ss-EPI R = 1**
- ↗ susceptibility artifact
- ↗ EC induced distortion

MD
FA

b=0 | direction 1 | direction 2
direction 3 | direction 4 | direction 5
direction 6 | direction 7 | direction 8
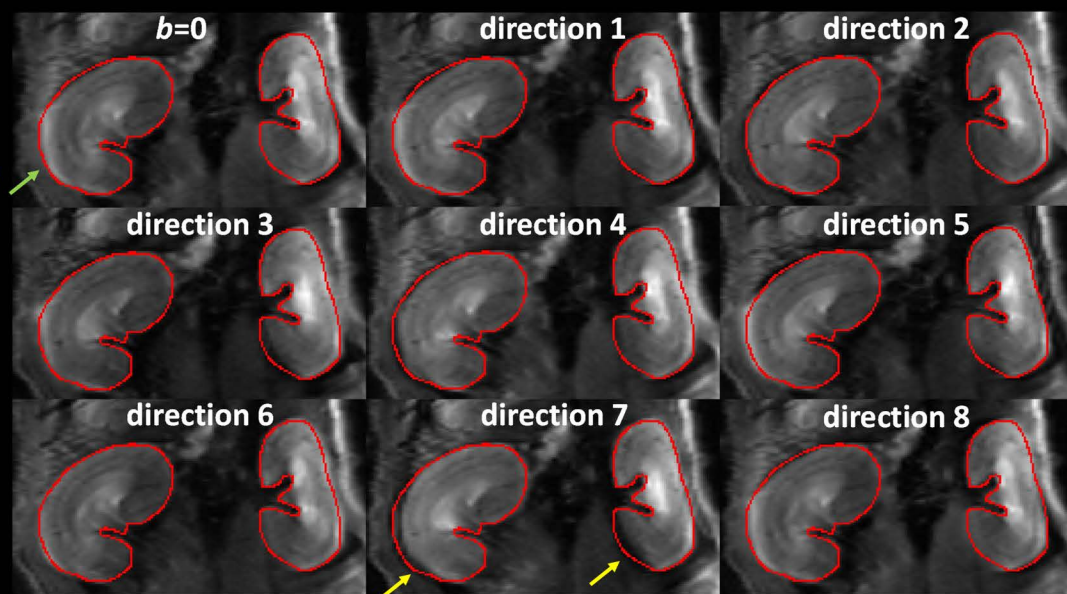
(B) **ss-EPI R = 2**
- ↗ susceptibility artifact
- ↗ EC induced distortion

MD
FA

b=0 | direction 1 | direction 2
direction 3 | direction 4 | direction 5
direction 6 | direction 7 | direction 8
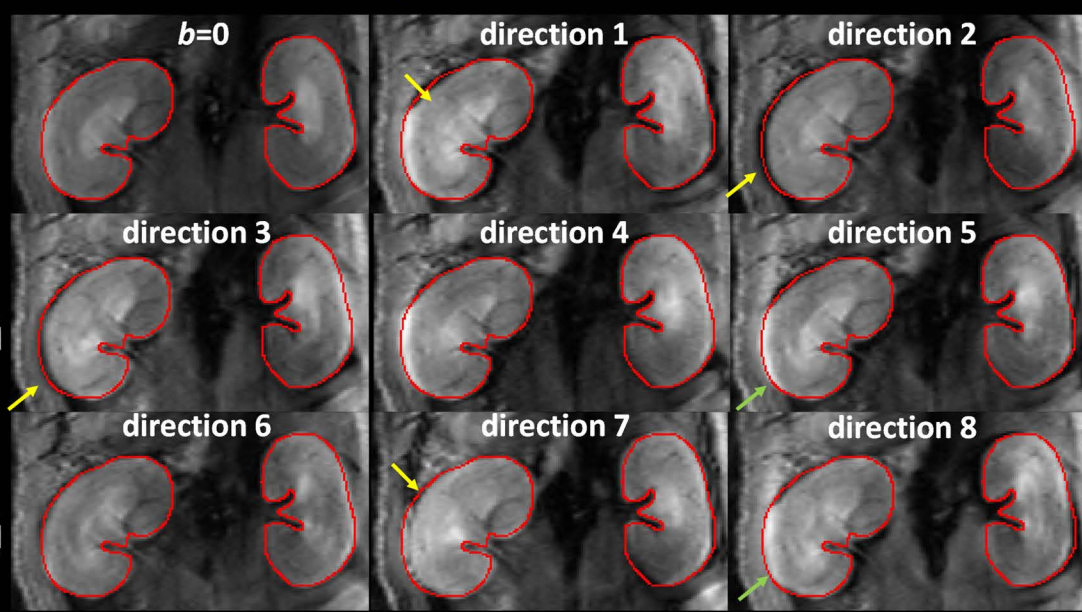
(C) **4-shot EPI**
- ↗ susceptibility artifact
- ↗ EC induced distortion

MD
FA

b=0 | direction 1 | direction 2
direction 3 | direction 4 | direction 5
direction 6 | direction 7 | direction 8